Catalysis Science & Technology

Accepted Manuscript

ROYAL SOCIETY OF CHEMISTRY

www.rsc.org/catalysis

Catalysis Science & Technology

PAPER

Promotional Role of Additive La on the NO Oxidation Performance of $SmMn_2O_5$ Mullite Catalyst

Received 00th January 20xx,
Accepted 00th January 20xx

DOI: 10.1039/x0xx00000x

www.rsc.org/

Zijian Feng,[a] Jianqiang Wang,[b] Xiao Liu[c], Yanwei Wen[a], Rong Chen[c], Hongfeng Yin[d], Meiqing Shen*[b] and Bin Shan*[a]

A series of $La_xSm_{1-x}Mn_2O_6$ (x=0, 0.1, 0.3, 0.5) catalysts were synthesized through a co-precipitation method, the catalytic activity of NO oxidation was enhanced with La substitution, and the maximum activity was achieved at x=0.3. XRD and HRTEM results revealed the formation of multiphase oxide as well as the interface structure between mullite ($SmMn_2O_5$) phase and Mn-rich perovskite ($La_{0.96}MnO_{3.05}$) phase. The main impact of different La/Sm molar ratios is the amount of surface adsorbed oxygen (O_{ads}) and surface Mn^{4+} ions as revealed by XPS results. The NO oxidation performance was enhanced through La addition by promoting the decomposition of nitrate/nitrite species and desorption of NO_2, improving the reducibility of surface adsorbed oxygen, as determined by the H_2-TPR, NO+O_2-TPRD and *in-situ* DRIFTS studies. Mono-, bi-dentate and bridged nitrates formed on the surface were determined to be primary reaction intermediates.

1. Introduction

Lean-burn diesel engines with high air/fuel ratio are attracting much attention due to their higher fuel efficiency. However, high oxygen content in the exhaust emission makes it difficult to remove nitrogen oxides (NO_x) which can result in detrimental environmental pollutions such as photochemical smog, acid rain, and ozone depletion.[1-3] In order to minimize the NO_x pollutants and meet increasingly stringent automotive emission standards, various devices and technologies have been developed, among which selective catalytic reduction (SCR) and NO_x storage reduction (NSR) are two mainstream solutions in auto exhaust treatment industry.[4-6] In both processes, NO_2 plays a key role due to its stronger oxidizing capacity and easiness of being absorbed and trapped by catalysts than NO. In particular, in the so called fast SCR process, $2NH_3+NO+NO_2 \rightarrow 2N_2+3H_2O$,[7,8] the highest efficiency requires with an equal amount of NO_2 and NO in the gas mixture. In addition, as an effective after-treatment technology to reduce the amount of released soot, the diesel particulate filters (DPFs) is widely used and a continuous DPF regeneration takes place by the action of NO_2, as NO_2 gets stronger oxidizability than O_2.[9] Since the direct downstream emission from a diesel engine has NO (~90%) as the major component, the NO oxidation to NO_2 is a critical step in improving the $DeNO_x$ and DPF regeneration efficiency.

Platinum group metal (PGM) catalysts have been widely used for the oxidation of NO due to their good performance. However, high cost and poor thermal stability of PGM limit its wider application.[10,11] So far, a substantial amount of work has been undertaken in search for catalysts based on metal oxides as alternatives to traditional PGM catalysts. Transition metal oxides such as MnO_x and Co_3O_4 have been investigated for NO oxidation, but the conversion efficiency has been found to be unsatisfactory.[8,12-14] Meanwhile, perovskite-type oxides have also been studied extensively since 1970s, with both un-substituted[15-18] and substituted[11,19-22] systems showing great promise as alternative emission catalysts. More recently, $SmMn_2O_5$ mullite and mullite based oxides were discovered and applied for NO oxidation as candidates for commercial PGM catalysts.[23,24] More specifically, the mixed phase $SrCeSmMn_7O_{14.83}$ catalyst possesses highest conversion about 88% at above 300 °C, much higher than the commercial Pt catalyst. It has been shown that $SmMn_2O_5$ is the main source of activity and further enhanced through co-existence of other metal oxide components, which is not uncommon in mixed phase oxides.[25-28]

Over the past years, it has been demonstrated that addition of hetero-atoms in metal oxides is an effective way of promoting their catalytic activity. Chen et al. showed that the activity of structurally modified non-stoichiometric perovskite La_xMnO_3 increases with decreasing La content.[18] Wang et al. investigated a B-site substituted perovskite, $LaMn_{1-y}Co_yO_3$, the increased activity was attributed to the altered Mn^{4+} and activated oxygen species resulted from the synergetic effect between cobalt and manganese.[19] Kim et al. reported superior performance of Sr-doped

[a] State Key Laboratory of Material Processing and Die and Mould Technology and School of Materials Science and Technology, Huazhong University of Science and Technology, Wuhan 430074, China.
Email: bshan@mail.hust.edu.cn
[b] School of Chemical Engineering and Technology, Tianjin University, 92 Weijin Road, Nankai District, Tianjin 300072, China.
Email: mqshen@tju.edu.cn
[c] State Key Laboratory of Digital Manufacturing Equipment and Technology and School of Mechanical Science and Engineering, Huazhong University of Science and Technology, Wuhan 430074, Hubei, China.
[d] Division of Fuel Cell & Energy Technology, Ningbo Institute of Material Technology and Engineering, Chinese Academy of Sciences, Ningbo 315201, Zhejiang, China.
†Electronic Supplementary Information (ESI) available: Detailed kinetic tests conditions, catalytic performance of individual oxide, NO-TPD results and DRIFTS study of catalysts, etc.. See DOI: 10.1039/x0xx00000x

$LaCoO_3$ perovskite catalyst in NO oxidation compared to a Pt based commercial diesel oxidation catalyst (DOC).[11,20] Moreover, metal oxides with La addition have also been investigated for reducing NO_x and carbon soot from the tail-pipe exhaust. W. Y. Hernández et al. prepared La doped CeO_2 and the research showed that the sample exhibited higher catalytic activity for CO oxidation due to the additional formation of oxygen vacancy.[29] La modified TiO_2 [30] and CeO_2 [31] were studied for soot oxidation, the enhanced catalytic activity was attributed to the increase of the lability of lattice oxygen and improved redox properties of CeO_2. Overall, the addition of rare earth elements such as La into transition metal oxides generally provides beneficial influence on the activity and thermal stability, as well as enhanced oxygen storage capacity. However, the application of La addition and its effect on the activity in the recently discovered $SmMn_2O_5$ mullite is still lacking to the best of our knowledge.

We present here a systematic study of the synthesis, characterization and performance of multiphase oxides based on $SmMn_2O_5$ mullite with La addition. A series of $La_xSm_{1-x}Mn_2O_\delta$ (x=0, 0.1, 0.3 and 0.5) catalysts were synthesized using co-precipitation method. The enhancement of catalytic activity for NO oxidation was observed among La modified samples, and the sample with the La/La+Sm molar ratio of 0.3 exhibited the best catalytic performance with low activation energy. With gradual increase of La concentrations, a multiphase catalyst with mullite ($SmMn_2O_5$) and non-stoichiometric perovskite ($La_{0.96}MnO_{3.05}$) as dominant phases was obtained as determined by the XRD and HRTEM characterizations. All the samples showed similar lump-like shape of morphology. The content of surface adsorbed oxygen species and surface Mn^{4+} increased after La introduction as revealed by the XPS characterization. The enhanced catalytic activity can be primarily attributed to the facile decomposition of nitrate/nitrite species and easier NO_2 desorption as illustrated by the $NO+O_2$-TPRD and DRIFTS studies, the surface adsorbed oxygen with improved reducibility as confirmed by H_2-TPR experiment contributed as well.

2. Experimental section

2.1. Catalyst preparation

La containing mullite-perovskite multiphase catalysts were prepared following the co-precipitation procedure as described in literature.[23] Briefly, samples of $La_xSm_{1-x}Mn_2O_\delta$ (x=0, 0.1, 0.3, 0.5) were prepared by dissolving appropriate amounts of $La(NO_3)_3 \bullet 6H_2O$, $Sm(NO_3)_3 \bullet 6H_2O$, $Mn(NO_3)_2$ (50wt.% in H_2O) in deionized water using Pluronic F127 as a non-ionic surfactant, and with adequate stirring at room temperature. Then adding into a 25% solution of tetramethyammonium hydroxide (TMAH) to increase the pH to 9-10, followed by the drop wise addition of 30% hydrogen peroxide (H_2O_2) (20-50% excess with regard to Mn) using octanol as a defoaming agent. The mixture was then stirred for 2 hours at room temperature and filtered to get the precipitate. Subsequently the precipitate was dried at 100 °C overnight and grinded to get the powder as precursor. Finally the precursor was calcined at 500 °C for 8 hours and followed by 8 hours at 800 °C in static air atmosphere. In this paper, catalysts with the formula $La_xSm_{1-x}Mn_2O_\delta$ (x=0, 0.1, 0.3, 0.5) are designated as LSM10×x. For example, $La_{0.1}Sm_{0.9}Mn_2O_\delta$ is abbreviated as LSM1.

The reference sample 2 wt.% Pt on γ-Al_2O_3 (Aladdin) was prepared by the incipient wetness method using $Pt(NO_3)_2$ (15 wt.% in H_2O, Aladdin) as precursor, calcined at 500 °C for 2 hours.

The LSM0 and LSM3 samples were hydrothermal aged and pre-sulfureted to evaluate their susceptibility to hydrothermal aging and sulfur poisoning. The hydrothermal aging conditions were set to 10 hours at 820 °C in 10% H_2O with air as balance and the total flow rate was set to 1000 ml/min. The sulfur poisoning conditions were 30 minutes at 300 °C in 200 ppm SO_2, 10% H_2O with air as balance and the total flow rate was set to 1000 ml/min.

2.2. Catalyst characterization

Phase identification of the fresh catalysts was carried out by X-ray diffraction (XRD), recorded on an analytical X'pert PRO diffractometer, using Cu Ka radiation with λ = 1.5406 Å in the 2θ ranging from 10 ° to 60 °. Phase recognition was obtained by comparison to standard JCPDS files. The Brunauer-Emmett-Teller (BET) specific surface area (m^2/g) measurements were determined by N_2 absorption at 77 K using Micromeritics ASAP 2020M physisorption analyzer. Prior to measurement, the samples were degassed at 300 °C under vacuum overnight. The scanning electron microscopic (SEM) images of the catalysts were recorded on a field-emission scanning electron microscopy (FE-SEM, FEI, Nova NanoSEM 450 microscope). Transmission electron microscopy (TEM) and high-resolution transmission microscopy (HRTEM) images were analyzed with a JEM 2100 microscope operated at 200 kV.

The X-ray photoelectron spectroscopy (XPS) measurements were conducted on AXIS ULTRADLD Multifunctional X-ray Photoelectron Spectroscope with an Al Kα radiation source at room temperature and the base pressure was 10^{-7} Pa (10^{-9} Torr). The starting angle of the photoelectron was set at 90 °. Fresh samples were used to conduct this experiment. All binding energies were calibrated internally by the carbon deposit C 1s binding energy (BE) at 284.8 eV.

50 mg sample was used in H_2 temperature programmed reduction (TPR) measurements on a FINESORB-3010E instrument (Zhejiang Finetec Co.). TPR profiles were recorded using a 10% H_2/Ar mixture. Prior to reduction, the sample was pretreated at 500 °C for 30 minutes in a stream of 10% O_2/N_2 (100 ml/min) and then cooled down to room temperature. The temperature was retained at room temperature for 30 minutes then increased to 800 °C at a rate of 5 °C/min, and kept at 800 °C for 30 minutes under the H_2/Ar flow at 50 ml/min. The variation of H_2 concentration in the outlet gas was continually monitored by a thermal conductivity detector (TCD), and a water trap removed moisture from the TPR effluent stream before the TCD.

The temperature programmed reaction and desorption (TPRD) of $NO+O_2$ experiments were carried out on a FINESORB-3010E instrument (Zhejiang Finetec Co.). 50 mg of sample was used in each $NO+O_2$-TPRD measurement. The adsorption/reaction of ($NO+O_2$) on the catalyst sample was carried out at 150 °C with a flow of 400 ppm NO, 10% O_2 in N_2 balance (150 ml/min) for 1 hour followed by purging with a N_2 flow (200 ml/min) at the same temperature for 1 hour. The catalyst was then heated up to 800 °C

at a rate of 5 °C/min. The composition of the desorbed gas was continuously recorded with a chemiluminescence NO_x analyzer (EcoPhysics, CLD822Mh), which can detect NO and NO_2 simultaneously with a detection limit of 0.25 ppm.

The temperature programmed desorption (TPD) of NO experiments were carried out on a FINESORB-3010E instrument (Zhejiang Finetec Co.). 50 mg of sample was used in each NO -TPD measurement. The adsorption of NO on the catalyst sample was carried out at room temperature with a flow of 500 ppm NO in N_2 balance (150 ml/min) for 1 hour followed by purging with a N_2 flow (200 ml/min) at the same temperature for 1 hour to eliminate weakly physical adsorbed NO on the catalysts. The catalyst was then heated up to 500 °C at a rate of 5 °C/min. The concentration of desorbed NO was continuously recorded with a chemiluminescence NO_x analyzer (EcoPhysics, CLD822Mh). The detailed results were given and discussed in supplementary material.

Diffuse reflectance infrared Fourier transform (DRIFT) spectra were obtained with a resolution of 4 cm^{-1} in the range of 1000-4000 cm^{-1}, using an FT-IR (Thermo Scientific Nicolet 6700) equipped with an MCT detector and a DRIFT cell (Pike). Prior to each FT-IR experiment, the sample was pretreated at 500 °C for 30 minutes in a flow of 10% O_2 in N_2 balance at 100 ml/min. The IR spectra were then obtained under the flow of 400 ppm NO, 0% or 10% O_2 and N_2 balance at 150 ml/min from 150 °C to 300 °C.

2.3. Catalytic activity testing

The catalysts (0.2 g) were tested in a U-type vertical quartz tubular reactor with 5 mm internal diameter operated at atmospheric pressure, with the temperature measured by a K-type thermocouple. The catalysts were placed in the middle of the reactor between two clogs of quartz wool. The gases were fed using a series of mass flow controllers. The reaction gas contained 400 ppm NO, 10% O_2, 3% H_2O and N_2 as the balance. The total flow rate was 600 ml/min, corresponding to a gas hour space velocity (GHSV) of about 90,000 h^{-1}. The effluent gas was analyzed by using a Fourier transform infrared (FTIR) spectrometer (MKS, MultiGas 2030). The furnace was ramped up at 5 °C/min rate from room temperature to 400 °C. The conversion of NO, X_{NO} (%), was defined as the percentage of NO feed that has reacted, and it was calculated according to Eq. (1):

$$X_{NO}(\%) = \frac{C_{NO,in} - C_{NO,out}}{C_{NO,in}} \times 100, \quad (1)$$

where $C_{NO,in}$ is the volumetric concentration of NO in the inlet gas and $C_{NO,out}$ is the volumetric concentration of NO in the outlet gas.

The NO oxidation kinetic study was carried out with a flow rate set to 400 ml/min, under which condition the diffusion effect could be eliminated (Fig. S1). 25 mg meshed (80-100 mesh) catalysts were used for each experiment in order to eliminate the internal diffusion effect (Fig. S2).[18,32,33] The samples were pretreated in 10% O_2/N_2 (100 ml/min) at 500 °C for 30 minutes. The steady-state NO oxidation experiments were performed using a reactant gas mixture containing 400 ppm NO, 10% O_2 and N_2 as the balance. The typical time to achieve a steady-state at each temperature was 30 minutes. The turnover frequencies (TOFs) of NO oxidation over the catalyst were normalized to NO adsorption sites and calculated according to Eq. (2):

$$TOF_{NO}(s^{-1}) = X_{NO} Q C_f / W N_{ad}, \quad (2)$$

where Q is the volumetric flow rate (ml/s) and C_f is the feed concentration of NO (mol/ml). W is the weight of the catalyst employed (g). N_{ad} is the adsorbed amount of NO (mol/g) below 200 °C (Table S2). To determine the activation energy (Ea), temperature was varied from 160 °C to 220 °C to ensure that the NO conversion is always lower than 15%, at which condition the inhibition effect of NO_2 on the NO oxidation reaction has been kept negligible (Fig. S3), and Ea was calculated from the slope of the Arrhenius-type plot of the oxidation TOFs of NO.

3. Results and discussion

3.1 NO oxidation activity of La substituted samples

Fig. 1a presents the conversions of NO as a function of the reaction temperature over the fresh catalysts for this series of samples with different additive La concentration. At low temperatures the NO oxidation was kinetically limited and the conversion was low. With temperature rising, the activity gradually increased, approaching the thermodynamic limit. Among these catalysts, pure $SmMn_2O_5$ showed activity above 100 °C and obtained a maximum conversion of 78% at 320 °C. By addition of La, enhancement of the catalytic activity for NO oxidation can be clearly observed. All La containing samples showed higher NO conversion than pure $SmMn_2O_5$ sample in the temperature range of 100-300 °C and the maximum activity point shifted from 320 °C to a lower temperature of 290 °C. In

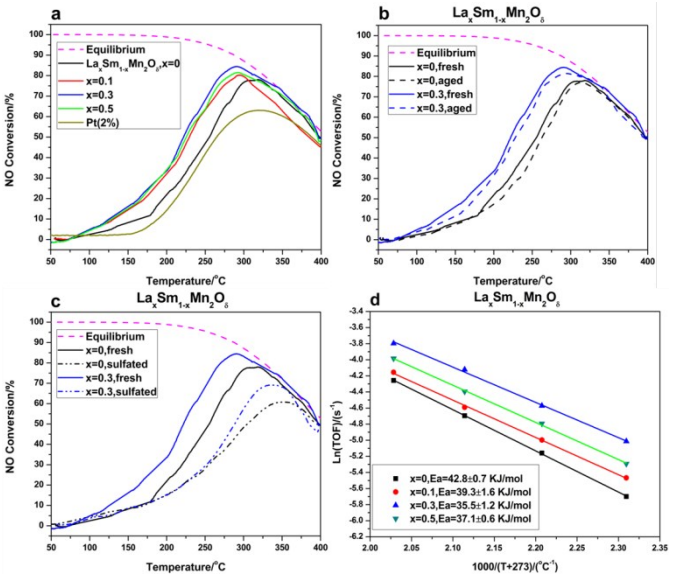

Fig. 1 a: Activities of $La_xSm_{1-x}Mn_2O_\delta$ (x=0, 0.1, 0.3, 0.5) fresh samples for NO oxidation; b: Activities of hydrothermal aged $La_xSm_{1-x}Mn_2O_\delta$ (x=0, 0.3); c: Activities of sulfated $La_xSm_{1-x}Mn_2O_\delta$ (x=0, 0.3); d: Arrhenius plots for the catalysts based on TOFs in the temperature range of 160-220 °C.

addition, all samples achieved higher activity than the reference precious metal sample, i.e. 2wt. % Pt on γ-Al_2O_3, which had a max conversion of 60% at around 330 °C. It is worth mentioning that the LSM3 catalyst exhibited the best performance, where the NO conversion started at temperatures as low as 100 °C, and obtained a maximum conversion of 85% at 290 °C. The catalytic performance is in the order of LSM3＞LSM5＞LSM1＞LSM0. LSM3 even showed the maximum conversion (91%) at about 255 °C without H_2O in the feed stream (Fig. S5), lower than reported mixed phase oxides $SmSrCeMn_7O_{14.83}$.[23] LSM0 and LSM3 samples were hydrothermal aged and pre-sulfureted as representatives to further investigate their susceptibility to hydrothermal aging and sulfur poisoning. The catalytic activities of LSM0 and LSM3 samples were maintained after hydrothermal aging as shown in Fig. 1b, the highest conversion slightly decreased to 77% and 82% for LSM0 and LSM3, respectively, indicating a strong hydrothermal resistance of mixed phase oxides. And LSM3 still exhibited better NO oxidation performance than LSM0 after hydrothermal aging in the whole temperature range. As for the pre-sulfureted LSM0 and LSM3 samples, we can see from Fig. 1c the NO oxidation activities both decreased considerably for the highest conversion of LSM0 and LSM3 samples decreased to 61% at 360 °C and 70% at 330 °C, respectively, implying its susceptibility to sulfur poisoning is to be further improved like many other metal oxides.

In an effort to compare the catalysts performance based on TOFs, NO desorption amount below 200 °C was considered as bonding to the active sites and quantified (Table S2).[34,35] The TOFs calculated as (mol NO converted/time)/(mol NO adsorbed) with temperature over the $La_xSm_{1-x}Mn_2O_\delta$ series catalysts are presented in Fig. 1d. The La modified catalysts exhibited higher NO oxidation TOFs than pure $SmMn_2O_5$ with LSM3 presenting the highest TOFs among the samples, which is consistent with the activity performance. The apparent activation energy for LSM samples as determined in the temperature range of 160-220 °C followed the sequence: LSM0 (42.8 kJ/mol) ＞LSM1 (39.3 kJ/mol) ＞LSM5 (37.1 kJ/mol) ＞LSM3 (35.5 kJ/mol). The lower NO oxidation activation energy of LSM3 catalyst indicates the beneficial effect of La addition in the $La_xSm_{1-x}Mn_2O_\delta$ composite catalysts.

3.2 Physical properties

Fig. 2 shows the XRD patterns of the $La_xSm_{1-x}Mn_2O_\delta$ catalysts with the bar patterns of $SmMn_2O_5$ [52-1096] phase included. The orthorhombic structure of $SmMn_2O_5$ mullite was clearly observed without any segregated phases in the x=0 sample. The calcination condition (8 hours at 500 °C followed by 8 hours at 800 °C) is considered sufficient for getting well-crystallized mullite structure. When La was introduced into the mullite, a mixed-phase oxide and a change of mullite structure were observed, consistent with results reported earlier.[10,23,36] When x=0.1, the typical XRD peak intensity of the $SmMn_2O_5$ mullite slightly decreased, implying less amount of $SmMn_2O_5$ was generated. Moreover, the two main peaks at 28.7 ° and 30.6 ° standing for $SmMn_2O_5$ shifted to lower 2θ angles (inset in Fig. 2), indicating that a portion of larger radius La^{3+} (1.36 Å) than that of Sm^{3+} (1.24 Å)[37-39] had been doped into the lattice structure of mullite, in agreement with the d-spacing (211) enlargement of $SmMn_2O_5$ mullite as a result of lattice volume expansion listed in

Table 1 $d_{(211)}$ of mullite and BET surface areas in $La_xSm_{1-x}Mn_2O_\delta$ oxides

$La_xSm_{1-x}Mn_2O_\delta$	x=0	x=0.1	x=0.3	x=0.5
$d_{(211)}$ of mullite (Å)	2.922	2.938	2.952	2.953
BET surface areas (m^2/g)	15.70	7.73	15.27	18.34

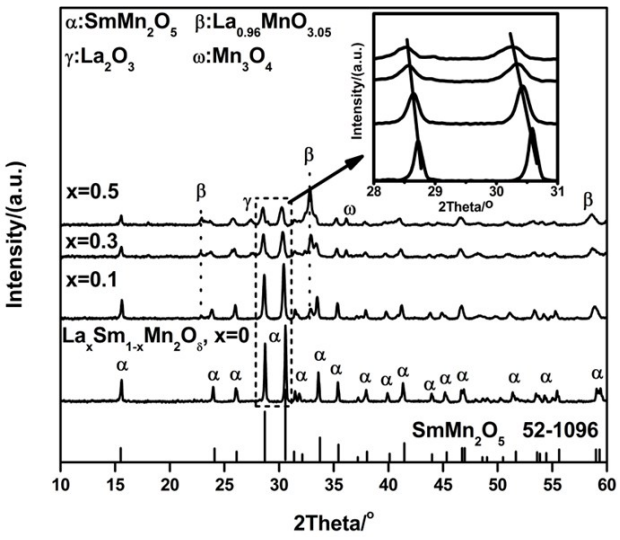

Fig. 2 XRD profiles of $La_xSm_{1-x}Mn_2O_\delta$ samples, x=0, 0.1, 0.3, 0.5.

Table 1. It is also worth noting that the appearance of two low intensity peaks at 22.9 ° and at 32.8 ° corresponds to the formation of non-stoichiometric Mn-rich perovskite-type $La_{0.96}MnO_{3.05}$ [89-0678] phase with rhombohedral structure. The generation of Mn-rich perovskite is reasonable as perovskite phase can be obtained at about 700 °C.[14,23] The origin of the formation of this Mn rich phase can also be attributed to the fixed molar ratio of Mn/(La+Sm) of 2 during the preparation process, as the remaining Mn was in excess to un-substituted La to form strictly stoichiometric perovskite. When x≥0.3, the XRD peak intensity of the $SmMn_2O_5$ mullite further decreased while the main peak intensity of $La_{0.96}MnO_{3.05}$ increased considerably. Small amount of La_2O_3 [22-0369] and Mn_3O_4 [24-0734] were also observed upon more La addition, their intensities increased with a concurrent loss of the mullite crystallinity. As for the LSM3 sample, which shows the best catalytic activity, its XRD spectrum in Fig.2 showed four crystalline phases: distorted mullite $SmMn_2O_5$, non-stoichiometric perovskite $La_{0.96}MnO_{3.05}$, hausmannite Mn_3O_4, and a small amount of La_2O_3.

The XRD results along with the expansion of d-spacing of $SmMn_2O_5$ (211) indicated that La was partially incorporated into the mullite structure along with the formation of non-stoichiometric Mn-rich perovskite, and the amount of perovskite phase increased with La molar ratio. The partial substitution of Sm^{3+} by La^{3+} would lead to the presence of structural defects and the formation of oxygen vacancies,[40,41] which were considered beneficial for NO oxidation.

BET specific surface area of the obtained samples was shown in Table 1. The specific surface area for LSM0 was 15.70 m^2/g. When

La was incorporated i.e. x=0.1, the specific surface area decreased to 7.73 m^2/g, which may be attributed to the aggregation of perovskite particles during the calcination process at 800 ^oC. The specific surface area increased for LSM3 and LSM5 samples, which had similar or higher specific surface area than the LSM0 sample. The addition of La caused a creation of multiphase with mullite-perovskite interface, as confirmed by XRD results and HRTEM image (Fig. 4b), generally, the multiphase content increases as raising La addition. Since LSM0 possessed a relatively high surface area, the higher surface area for LSM3 and LSM5 may be mainly attributed to the increased multiphase, preventing the aggregation of perovskite nanoparticles. The segregated La_2O_3 particles may also act as sintering barriers to inhabit the growth of grain when calcined at high temperature.[42-44] A similar trend has been also observed over the Sr, Ag substituted $LaMnO_3$ perovskite.[36,40]

SEM was employed to examine the morphology of the La containing composite catalysts with respect to their La content. In Fig. 3, the LSM samples showed the agglomerated lump-like shape of morphology, regardless of the La amount. LSM1 sample had the lowest specific surface area, with the particles aggregation clearly observed. The particle sizes of LSM0, LSM3 and LSM5 samples displayed by the SEM images were consistent with the BET measurements.

Since LSM3 sample exhibited the best catalytic performance among the samples. TEM and HRTEM images of LSM3 sample were taken and shown in Fig. 4. The particle size of as-prepared catalysts was in the range of 50 nm to 60 nm. Well-crystallized mullite-type $SmMn_2O_5$ (whose lattice fringe of (1 1 0) plane is 0.563 nm), perovskite-type $La_{0.96}MnO_{3.05}$ (whose lattice fringe of (1 1 0) plane is 0.273 nm) and the formation of interface structure between mullite and perovskite could be seen from the HRTEM image (Fig. 4b). These were in good agreement with the XRD results implying that the sample was multiphase composed. The (1 1 0) plane of $SmMn_2O_5$ is active for NO oxidation according to Wang's work.[23] Furthermore, Chen et al. found that Mn-rich perovskite showed

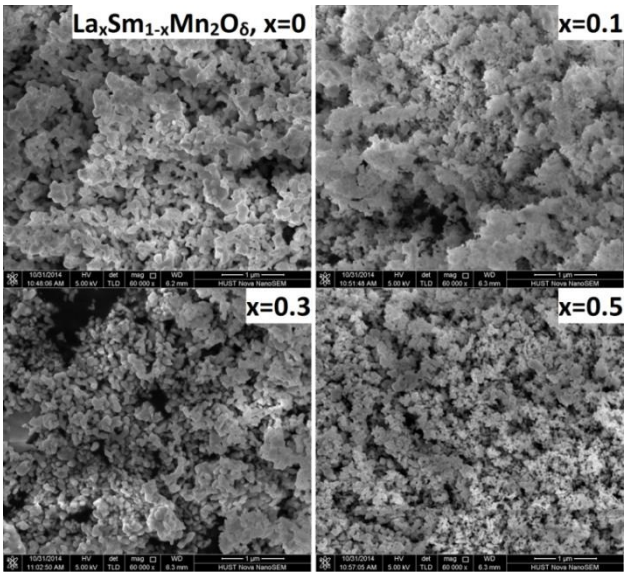

Fig. 3 SEM images of $La_xSm_{1-x}Mn_2O_\delta$ samples, x=0, 0.1, 0.3, 0.5.

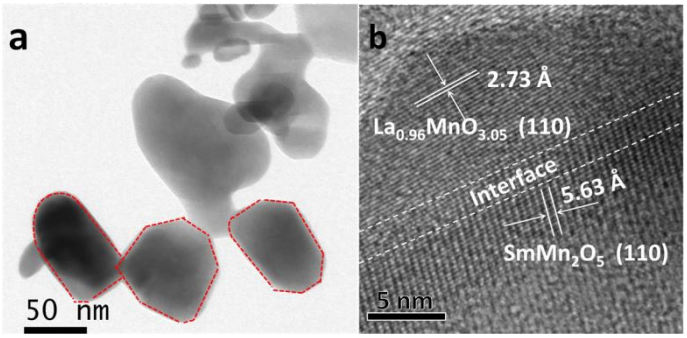

Fig. 4 TEM and HRTEM images of $La_{0.3}Sm_{0.7}Mn_2O_\delta$ (LSM3) sample. a: TEM image; b: HRTEM image.

better catalytic activity for NO oxidation than strictly stoichiometric $LaMnO_3$.[18] In our NO oxidation reaction, the activity of Mn_3O_4 and La_2O_3 showed only negligible conversion for NO oxidation below 400 ^oC (Fig. S4), these non-active oxides would not contribute much to the catalytic activity directly. The lower reaction rates of perovskite than mullite on the basis of surface area through 200-275 ^oC (Table S1) suggested the catalytically active sites were mainly mullite phase among the mixed phase oxides, the perovskite results in additional high-temperature (>300 ^oC) catalytic activity. The La containing mullite-perovskite composite oxides showed higher activity than individual component (Fig. S4), indicating a synergetic effect between the active mullite and perovskite phases.[25-28] The formation of defects and vacancies would lead to enhanced capacity of electron capture and release, resulting in better reducibility of catalysts and promoting the catalytic activity.

3.3 Surface chemical states of the La modified samples

XPS was used to reveal the chemical states and the relative abundance of the elements on the surface of LSM catalysts. Fig. 5a shows the XPS spectra of O 1s for the $La_xSm_{1-x}Mn_2O_\delta$ samples. There were two oxygen signals: lattice oxygen (O^{2-}) at 529.3-529.9 eV, and surface adsorbed oxygen (O_2^{2-}, O^- etc) at 531.0-531.4 eV.[36,40,45,46] The molar ratio of O_{ads}/O_{latt} was obtained by quantitative calculation of the corresponding peaks areas and is shown in Table 2. The O_{ads}/O_{latt} molar ratio has an initial increase with La addition, which can be attributed to the formation of additional oxygen vacancies resulted from the partial substitution of Sm by La, which attracts weakly bound oxygen species compared with lattice O^{2-} ions.[36,40] The generated non-stoichiometric perovskite $La_{0.96}MnO_{3.05}$ contributed as well. When further increasing La content, the formation of segregated non-active oxides, such as La_2O_3, Mn_3O_4 etc., would block the oxygen vacancies and lead to a decrease of O_{ads}/O_{latt} molar ratio. The slightly higher La/Sm molar ratio on the surface of La modified samples than theoretical value (Table 2) suggested the surface enrichment of La, which supported the deduction. Furthermore, as for LSM0 sample, the binding energy for lattice oxygen and surface oxygen was 529.13 eV and 531.02 eV, respectively. It is found that the binding energy shifted to 529.59 eV and 531.34 eV for LSM3 catalyst. The increase in the binding energy after the addition of La could be correlated to the presence of defects in oxides[45] and the chemical state change of surface oxygen, which may improve the ability of electron capture and release, leading to enhanced reducibility of surface oxygen.

Table 2 Surface atomic ratio of $La_xSm_{1-x}Mn_2O_\delta$

$La_xSm_{1-x}Mn_2O_\delta$	x=0	x=0.1	x=0.3	x=0.5
O_{ads}/O_{latt}	0.37	0.64	0.59	0.54
Mn^{4+}/Mn^{3+}	0.70	1.08	0.97	0.83
La/Sm	0	0.18	0.61	1.29

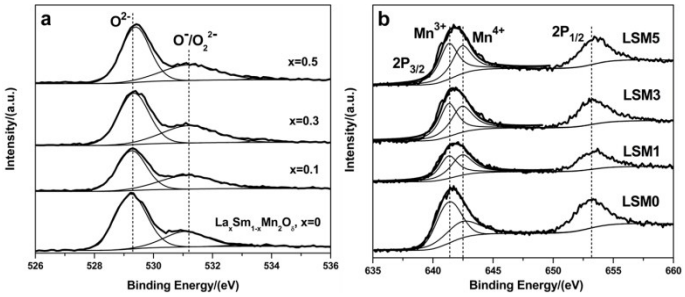

Fig. 5 XPS spectra of $La_xSm_{1-x}Mn_2O_\delta$ (x=0, 0.1, 0.3, 0.5) samples. a: O 1s spectra; b: Mn 2p spectra.

Fig. 5b shows the XPS spectra of Mn 2p. The Mn 2p profiles could be de-convoluted into two contributions referred to Mn^{3+} at 641.3-641.7 eV and Mn^{4+} at 642.2-643 eV,[40,47,48] respectively. The detailed Mn^{4+}/Mn^{3+} atomic ratio is summarized in Table 2. It could be seen from the table that with respect to the amount of La substitution, the concentration of Mn^{4+} follows similar trend as that of O_{ads}/O_{latt} molar ratio which is in agreement with previous reports.[49,50] Mn^{4+} was formed in both mullite and non-stoichiometric perovskite structures. After La addition, the O_{ads}/O_{latt} molar ratio increased for LSM1 due to the formation of additional vacancies adsorbing oxygen, while decreased for LSM3 and LSM5 as more segregated non-active oxides blocking the vacancies. When the vacancies were filled up with adsorbed oxygen and led to increased O_{ads}/O_{latt} molar ratio, the neighbouring Mn^{3+} would be oxidized into Mn^{4+} to balance the charge neutralization, resulting in higher Mn^{4+}/Mn^{3+} molar ratio, following the same sequence of O_{ads}/O_{latt}.[40,51,52] Partial oxidation of Mn^{3+} into unstable Mn^{4+} ions on the surface of the catalysts could produce more active sites of redox couples and lead to better catalytic performance than pure $SmMn_2O_5$ mullite. Since adsorbed surface oxygen is active in oxidation reactions, higher O_{ads} ratio would facilitate the oxidation of NO to some extent. Among the catalysts, all the La containing samples achieved higher percentage of adsorbed oxygen, and exhibited better performance than $SmMn_2O_5$ mullite. However, the LSM1 sample which got highest amount of oxygen had a low activity. It indicates that the catalytic activities of samples are not simply determined by adsorbed oxygen amount, the reducibility of adsorbed oxygen and NO_2 desorption behaviour would play crucial roles. Especially for the NO_2 desorption performance, which is proposed as the rate limiting step in NO oxidation for mullite catalysts.[23,24] These characterizations will be further discussed in the following parts.

3.4 Reducibility of the catalysts

In general, the reducibility and replenishment of surface oxygen species play a key role in NO oxidation. The easy reducible adsorbed oxygen would affect the $NO+O_{ads}$ reaction and further influence the catalytic activity. In order to investigate the reducibility of oxygen species on the surface of multiphase oxides, H_2-TPR experiments were carried out. Fig. 6 shows TPR profiles for the LSM series catalysts. In general, the H_2-TPR profiles of the LSM samples showed three reduction peaks, with a peak at below 400 °C, a shoulder close to 450 °C, and the last peak at around 650 °C, suggesting a multiple-step reduction process. Note that the catalyst samples were pretreated by O_2 before the TPR experiment. The first reduction profile can be assigned to the removal of surface adsorbed oxygen, which are the most weakly bound and active oxygen in the catalysts, followed by the reduction of Mn^{4+} to Mn^{3+} below 500 °C, and a third reduction peak above 600 °C resulted from the reduction of Mn^{3+} to Mn^{2+}.[40,53,54] In addition, it is noteworthy that the first reduction peak ascribed to the reduction of surface adsorbed oxygen moved to a lower temperature from 398 °C to 392 °C when La was introduced into the composite catalyst. The reduction temperatures further moved to 365 °C and 375 °C for LSM3 and LSM5 samples, respectively. The lower temperature suggested the easiness of reduction of surface adsorbed oxygen for La containing composite catalysts.

The differences in reducibility of different LSM series catalysts can be attributed to changes in the composition of catalysts with various La/Sm molar ratios. According to the XRD results, the La/Sm molar ratio showed significant effects on the molar ratio of perovskite/mullite, thus an appropriate perovskite/mullite ratio will lead to the reduction of the surface adsorbed oxygen at low temperatures. The excess oxygen on the surface of $La_{0.96}MnO_{3.05}$ is easier to be reduced than that of $SmMn_2O_5$ mullite forming more stable stoichiometric perovskite while the neighbouring mullite would reoxidize the reduced perovskite, leading to easier reducible

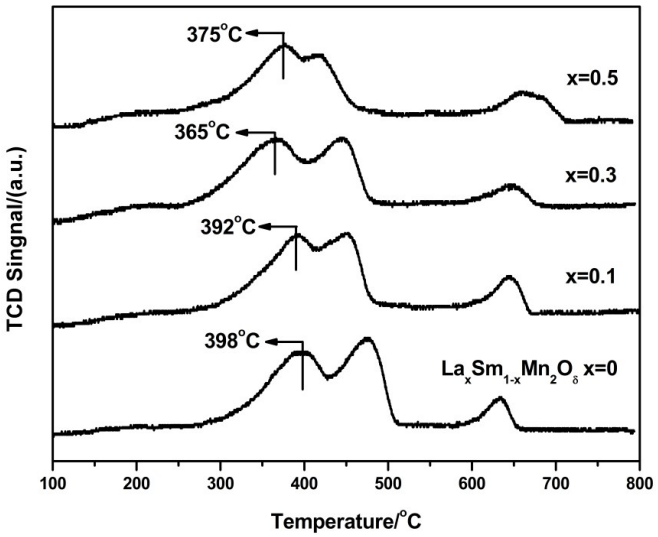

Fig. 6 H_2-TPR profiles of $La_xSm_{1-x}Mn_2O_\delta$ (x=0, 0.1, 0.3, 0.5) samples.

multiphase catalysts than pure mullite. The presence of $SmMn_2O_5$ combined with $La_{0.96}MnO_{3.05}$ would facilitate the mobility and activation of adsorbed oxygen, as indicated by the shift of binding energy of surface adsorbed oxygen on La containing catalysts, promoting the reducibility of LSM3 sample and resulting in better reactivity.[19,36,38] This promotion is less evident for LSM1 sample because fewer interfaces were formed due to small amount of perovskite. As for LSM5 sample, the content of mullite decreased with the concomitant formation of non-active oxides La_2O_3 and Mn_3O_4, which would block the active sites. The increased inert oxides resulted in worse reducibility of surface adsorbed oxygen than that of LSM3. As a result, La containing samples got improved reducibility of surface adsorbed oxygen and exhibited better NO oxidation performance, which is consistent with the trend in the reactivity of catalysts.[38,40,45] It is evident that the facile reducible surface adsorbed oxygen species played a key role in NO oxidation over mullite-perovskite multiphase oxides. The second consumption peak ascribed to the reduction of Mn^{4+} to Mn^{3+} clearly shifted to lower temperature when La content was increased up to 0.5, indicating easier reduction of Mn^{4+}. The easily reducible Mn^{4+} may arise from increased perovskite amount as $LaMnO_3$ has a lower reduction temperature of Mn^{4+} to Mn^{3+}.[15,18,38] The third reduction peak at above 600 °C shifted to higher temperature region when La was introduced, indicating the improved thermal stability attributed to the highly dispersed La_2O_3 oxide.[42-44]

3.5 ($NO+O_2$) TPRD and DRIFTS study of NO oxidation over La modified mullites

To further investigate the active surface species in LSM samples, the ($NO+O_2$) *in-situ* TPRD experiment was conducted for the analysis of the concentration of desorbed NO_x species. NO and NO_2 were the main desorption species as shown in Fig. 7. Note that the pretreatment was carried out at 150 °C, at which the conversion of NO was low, it is reasonable that more NO desorbed than NO_2. NO_2 desorption performance was foremost for it being proposed as the rate limiting step for mullite oxides in NO oxidation according to the literatures.[23,24] The desorption amount of NO_2 and NO increased for LSM1 catalyst than that of pure $SmMn_2O_5$, implying larger amount of NO_x was generated from decomposed surface nitrites/nitrates. The desorption amount of NO_2 further increased when increasing x to 0.3 and 0.5. While the NO_2 desorption temperature decreased slightly from 235 °C to 232 °C for LSM1 sample, further shifted to a lower temperature region to 209 °C for LSM3 sample, and 228 °C for LSM5 sample, respectively. The NO_2 desorption performance follows the similar trend as that of surface adsorbed oxygen reducibility, and a lower NO_2 desorption temperature for La containing catalysts will result in faster NO_2 formation on the surface of La-substituted mullite in the low-temperature region compared to that on pure $SmMn_2O_5$. With the lowest NO_2 desorption temperature, LSM3 catalyst exhibited the highest catalytic activity for NO oxidation. On the other hand, the trend of NO desorption behaviour follows the same trend as that of NO_2 desorption. We can see that NO_2 formation and desorption performance got improved through La substitution, indicating the better reactivity of active sites on multiphase catalysts, thus leading to higher TOF values for samples with various La loadings than that of pure mullite.

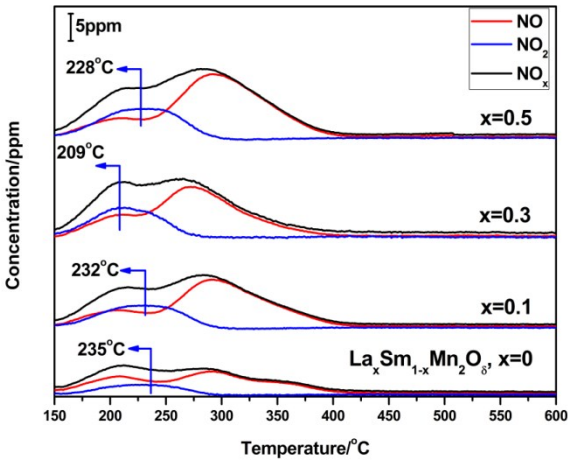

Fig. 7 ($NO+O_2$) profiles of $La_xSm_{1-x}Mn_2O_\delta$ (x=0, 0.1, 0.3, 0.5).

In-situ DRIFTS experiments were also performed at steady state in NO and $NO+O_2$ gas environments at 150 °C (Fig. 8a). Only the adsorption species with high stability would be present on the surface when the spectra were taken. NO adsorption on LSM samples was investigated first. Four types of the nitrate species, mono- , bridged- and bi-dentate nitrates on manganese oxides as well as Sm-nitrate, and mono-dentate Mn-nitrite can be formed on the surfaces of catalysts according to the literatures.[23,40,55,56] The formation of nitrates/nitrites resulted from the $NO+O_{ads}$ reaction acting as the first step in NO oxidation on catalysts. Moreover, when x≥0.3, a new band at 1340 cm^{-1} emerged and it can be assigned to the NO chelating on La_2O_3,[57,58] which is in accordance with the XRD results, indicating the existence of segregated La_2O_3 in LSM3 and LSM5 multiphase oxides. In comparison with the

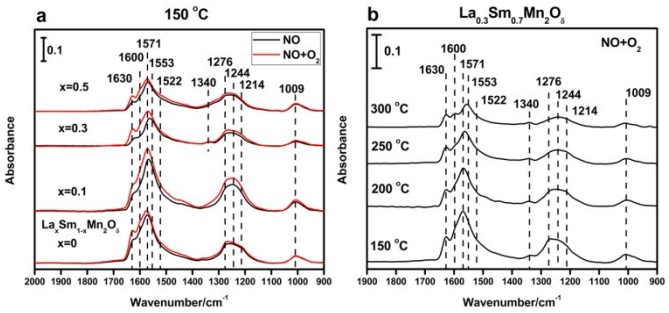

Mn bi-dentate nitrate: 1630 and 1571 cm^{-1}; Mn mono-dentate nitrate: 1522 and 1276 cm^{-1}; Mn bridged nitrate: 1214, 1244 and 1009 cm^{-1}; Mn mono-dentate nitrite: 1600 cm^{-1}; Sm nitrate: 1553 cm^{-1}; La_2O_3 NO chelating: 1340 cm^{-1}

Fig. 8 a: Evolution of DRIFTS spectra at 150 °C on $La_xSm_{1-x}Mn_2O_\delta$ (x=0, 0.1, 0.3, 0.5) samples during exposure to NO and $NO+O_2$ feed gases; b: DRIFT spectra of the $La_{0.3}Sm_{0.7}Mn_2O_\delta$ sample as a function of temperature. Feed: 400 ppm NO, 10% O_2 and N_2 balance. Temperature: 150-300 °C.

adsorption spectra with only NO flowing through the samples, intensities of bands positioned at 1630, 1600 and 1571 cm^{-1} increased when O_2 was introduced, which resulted from the restoration of consumed surface adsorbed oxygen, similar to the findings by Wang et al.[23] From these results, it could be deduced that bi-dentate Mn-nitrate and mono-dentate Mn-nitrite on the mullite surface were main reaction intermediates and the important role of surface oxygen in forming intermediates in NO oxidation. The IR bands due to nitrate/nitrite species on LSM0 and LSM1 were quite strong, indicating that $NO+O_{ads}$ reaction is fast enough on the surface. It is noteworthy that IR spectra intensities of LSM3 and LSM5 catalysts at 1630, 1600 and 1571 cm^{-1} decreased compared to LSM0 and LSM1 catalysts. This observation indicated that the main reaction intermediates may be destabilized after the introduction of La. The destabilization will induce the intermediates to be more easily decomposed to desorb NO_2 and accelerate the rate-limiting step in NO oxidation for mullite, which is in good agreement with the lower NO_2 desorption temperature as determined by the ($NO+O_2$) TPRD study. The easier NO_2 desorption in turn regenerated the surface active sites quickly to keep the reaction continue and further accelerated NO oxidation reaction rates. The promoted decomposition of nitrate/nitrite species and desorption of NO_2 may mainly be due to the generation of interface between mullite and non-stoichiometric perovskite. The performance got continually improved with formation of more interface as x increased to 0.3, beyond which some of the interface were blocked by segregated inert oxides and resulted in worse performance than x=0.3 sample.

The spectra in Fig. 8b reveal the effect of temperature on the IR spectra of $NO+O_2$ for the LSM3 sample. Fig. 8b suggests the formation of mono-, bridged- and bi-dentate nitrates on manganese oxides as well as the formation of Sm-nitrate, mono-dentate Mn-nitrite and NO chelating on La_2O_3 in the range of 150-300 ^oC. The significant decrease of the IR intensities of the mono-dentate and bi-dentate nitrates/nitrites when increasing the temperature, coupled with the intensity restoration of bands mentioned above and the NO_2 desorption from the catalyst surface as shown in Fig. 7 suggested that these nitrate/nitrite species are the key reaction intermediates in the oxidation of NO to NO_2 over mullite-perovskite multiphase catalysts. What's more, a higher percent of intensity decrease for LSM3 sample generally indicated easier conversion of reaction intermediates to NO_2 formation, and better specific cite reactivity (Fig. S7). The spectra intensity of chelating NO on La_2O_3 was constant in the whole temperature region, indicating that the chelating NO on La_2O_3 is not responsible for NO_2 formation, which is consistent with the activity test for La_2O_3 (Fig. S4).

Combining the evidences from XPS, H_2-TPR, $NO+O_2$-TPRD and *in-situ* DRIFTS experiments, the reaction pathways for oxidizing NO to NO_2 over $La_xSm_{1-x}Mn_2O_\delta$ (x=0.1, 0.3, 0.5) are proposed and depicted in Scheme 1, where some of surface adsorbed oxygen serve as active sites,[23,38,56] and the reaction pathways may involve more active surface oxygen bonding to the interface of non-stoichiometric perovskite and mullite, which is slightly different from pure mullite. In brief, NO is oxidized by active surface adsorbed oxygen firstly to form mono- (1600, 1522, 1276 cm^{-1}) and bi-dentate (1630, 1571 cm^{-1}) nitrates/nitrites (step 1), followed by

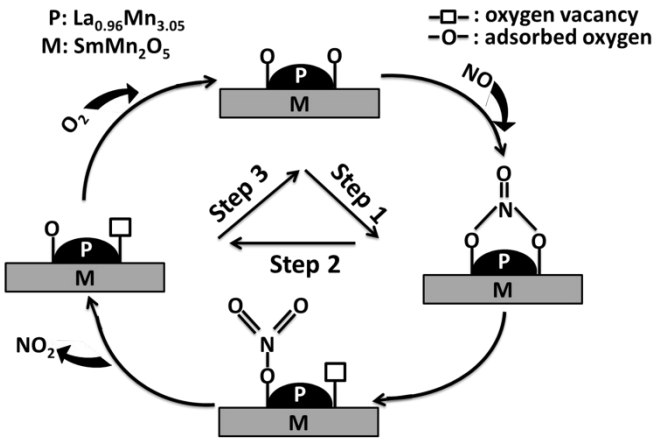

Scheme 1 Reaction pathways for NO oxidation on the surface of $La_xSm_{1-x}Mn_2O_\delta$.

its decomposition into NO_2 to generate the oxygen vacancies (step 2), and finally gas-phase oxygen adsorbs onto the oxygen vacancies to replenish surface adsorbed oxygen to complete the redox cycle (step 3), constituting the primary reaction pathway to oxidize NO to NO_2. Formation of the mullite/perovskite interface is beneficial to both the NO_2 desorption barrier reduction and improving the reducibility of adsorbed oxygen. The enhanced catalytic activity of NO oxidation for La substituted $SmMn_2O_5$ mullite is most relevant to the easiness of NO_2 desorption coming from the decomposition of surface nitrate/nitrite species, which is proposed as the rate limiting step in NO oxidation for mullite catalysts.[23,24] The easily reducible surface adsorbed oxygen facilitated the easier $NO+O_{ads}$ reaction (step 1), and together the easier NO_2 desorption regenerates the surface active sites quickly (step 2) to keep the reaction continue and further accelerate NO oxidation reaction rates. Therefore, the NO oxidation catalytic activity for La substituted mullite oxides is improved with accelerated reaction rates in the step 1 and 2 process.

4. Conclusions

La modified $SmMn_2O_5$ mullite oxides ($La_xSm_{1-x}Mn_2O_\delta$) synthesized using co-precipitation method were applied to catalyze the NO oxidation reaction. Multiphase catalysts based on mullite and perovskite were obtained after La introduction. All samples with additive La got enhanced catalytic performance, among which $La_{0.3}Sm_{0.7}Mn_2O_\delta$ catalyst exhibited the highest activity with a maximum conversion of 85% at about 290 ^oC as well as high hydrothermal resistance. The ratios of O_{ads}/O_{latt} and Mn^{4+}/Mn^{3+} on the composite catalysts increased and the surface adsorbed oxygen achieved better reducibility through La substitution. The enhanced catalytic performance was mainly attributed to the decreased thermal stability of major reaction intermediates, i.e. mono- and bi-dentate nitrates/nitrites on catalysts surface, facilitating NO_2 desorption and finally promoting NO oxidation as revealed by *in-situ* DRIFTS characterization. The easily reducible surface adsorbed oxygen contributed as well.

Acknowledgements

This work is supported by the National Basic Research Program of China (2013CB934800), National Natural Science Foundation of China (51575217, 51572097), Fundamental Research Funds for the Central Universities, HUST (2014TS037), the Hubei Province Funds for Distinguished Young Scientists (2014CFA018 and 2015CFA034). Rong Chen acknowledges the Thousand Young Talents Plan, the Recruitment Program of Global Experts and Program for Changjiang Scholars and Innovative Research Team in University (NO.: IRT13017). The authors also would like to acknowledge the technology support from the Analytic Testing Center of HUST.

Notes and references

1 W. P. Shan and H. Song, *Catal. Sci. Technol.*, 2015, **5**, 4280-4288.
2 X. G. Li, Y. H. Dong, H. Xian, W. Y. Hernandez, M. Meng, H. H. Zou, A. J. Ma, T. Y. Zhang, Z. Jiang, N. Tsubaki and P. Vernoux, *Energ. Environ. Sci.*, 2011, **4**, 3351-3354.
3 H. Kannisto, K. Arve, T. Pingel, A. Hellman, H. Harelind, K. Eranen, E. Olsson, M. Skoglundh and D. Y. Murzin, *Catal. Sci. Technol.*, 2013, **3**, 644-653.
4 F. D. Liu, Y. B. Yu and H. Hong, *Chem. Commun.*, 2014, **50**, 8445-8463.
5 H. E. van der Bij and B. M. Weckhuysen, *Chem. Soc. Rev.*, 2015, **44**, 7406-7428.
6 G. Liu and P. X. Gao, *Catal. Sci. Technol.*, 2011, **1**, 552-568.
7 L. Olsson and E. Fridell, *J. Catal.*, 2002, **210**, 340–353.
8 M. F. Irfan, J. H. Goo and S. D. Kim, *Appl. Catal., B*, 2008, **78**, 267-274.
9 Q. Shen, M. F. Wu, H. Wang, C. He, Z. P. Hao, W. Wei and Y. H. Sun, *Catal. Sci. Technol.*, 2015, **5**, 1941-1952.
10 Y. X. Wen, C. B. Zhang, H. He, Y. B. Yu and Y. Teraoka, *Catal. Today*, 2007, **126**, 400-405.
11 C. H. Kim, G. S. Qi, K. Dahlberg and W. Li, *Science*, 2010, **327**, 1624-1627.
12 Z. B. Wu, N. A. Tang, L. Xiao, Y. Liu and H. C. Wang, *J. Colloid Interface Sci.*, 2010, **352**, 143–148.
13 Z. Ren, Y. B. Guo, Z. H. Zhang, C. H. Liu and P. X. Gao, *J. Mater. Chem. A*, 2013, **1**, 9897-9906.
14 G. S. Qi and R. T. Yang, *J. Catal.*, 2003, **217**, 434-441.
15 J. H. Chen, M. Q. Shen, X. Q. Wang, J. Wang, Y. G. Su and Z. Zhao, *Catal. Commun.*, 2013, **37**, 105–108.
16 X. Liu, Z. Z. Chen, Y. W. Wen, R. Chen and B. Shan, *Catal. Sci. Technol.*, 2014, **4**, 3687-3696.
17 Z. Z. Chen, C.H. Kim, L. T. Thompson and W. F. Schneider, *Surf. Sci.*, 2014, **619**, 71-76.
18 J. H. Chen, M. Q. Shen, X. Q. Wang, G. S. Qi, J. Wang and W. Li, *Appl. Catal., B*, 2013, **134–135**, 251–257.
19 J. Wang, Y. G. Su, X. Q. Wang, J. H. Chen, Z. Zhao and M. Q. Shen, *Catal. Commun.*, 2012, **25**, 106–109.
20 S. O. Choi, M. Penninger, C. H. Kim, W.F. Schneider and L. T. Thompson, *ACS Catal.*, 2013, **3**, 2719−2728.
21 C. Zhou, X. Liu, C. Z. Wu, Y. W. Wen, Y. J. Xue, R. Chen, Z. L. Zhang, B. Shan, H. F. Yin and W. G. Wang, *Phys. Chem. Chem. Phys.*, 2014, **16**, 5106-5112.
22 C. Zhou, Z. J. Feng, Y. X. Zhang, L. J. Hu, R. Chen, B. Shan, H. F. Yin, W. G. Wang and A. S. Huang, *RSC Adv.*, 2015, **5**, 28054-28059.
23 W. C. Wang, G. McCool, N. Kapur, G. Yuan, B. Shan, M. Nguyen, U. M. Graham, B. H. Davis, G. Jacobs, K. Cho and X. H. Hao, *Science*, 2012, **337**, 832-835.
24 Z. Z. Chen, X. Liu, K. Cho, R. Chen and B. Shan, *ACS Catal.*, 2015, **5**, 4913-4926.
25 J. L. Shi, *Chem. Rev.*, 2013, **113**, 2139 −2181.
26 L. Chen, J. H. Li and M. F. Ge, *J. Phys. Chem. C*, 2009, **113**, 21177-21184.
27 C. W. Yen, M. L. Lin, A. Q. Wang, S. A. Chen, J. M. Chen and C. Y. Mou, *J. Phys. Chem. C*, 2009, **113**, 17831-17839.
28 Q. L. Yao, Z. H. Lu, Y. Q. Wang, X. S. Chen and G. Feng, *J. Phys. Chem. C*, 2015, **119**, 14167-14174.
29 W. Y. Hernández, O. H. Laguna, M. A. Centeno and J. A. Odriozola, *J. Solid State Chem.*, 2011, **184**, 3014–3020.
30 I. Atribak, I. Such-Basanez, A. Bueno-Lopez and A. G. Garcia, *Catal. Commun.*, 2007, **8**, 478–482.
31 A. Bueno-López, K. Krishna, M. Makkee and J. A. Moulijn, *J. Catal.*, 2005, **230**, 237-248.
32 J. J. Xue, X. Q. Wang, G. S. Qi, J. Wang, M. Q. Shen and W. Li, *J. Catal.*, 2013, **297**, 56-64.
33 S. T. Oyama, X. M. Zhang, J. Q. Lu, Y. F. Gu and T. Fujitani, *J. Catal.*, 2008, **257**, 1-4.
34 M. M. Yung, E. M. Holmgreen and U. S. Ozkan, *J. Catal.*, 2007, **247**, 356-367.
35 B. Thirupathi and P. G. Smirniotis, *J. Catal.*, 2012, **288**, 74-83.
36 S. Ponce, M. A. Peña and J. L. G. Fierro, *Appl. Catal., B*, 2000, **24**, 193–205.
37 R. D. Shannon, *Acta Cryst. A*, 1976, **32**, 751-767.
38 D. Y. Yoon, E. Lim, Y. J. Kim, J. H. Kim, T. Ryu, S. Lee, B. K. Cho, I. -S. Nam, J. W. Choung and S. Yoo, *J. Catal.*, 2014, **319**, 182–193.
39 P. Ciambelli, S. Cimino, S. De Rossi, M. Faticanti, L. Lisi, G. Minelli, I. Pettiti, P. Porta, G. Russo and M. Turco, *Appl. Catal., B*, 2000, **24**, 243–253.
40 A. Machocki, T. Ioannides, B. Stasinska, W. Gac, G. Avgouropoulos, D. Delimaris, W. Grzegorczyk and S. Pasieczna, *J. Catal.*, 2004, **227**, 282–296.
41 D. Jampaiah, K. M. Tur, S. J. Ippolito, Y. M. Sabri, J. Tardio, S. K. Bhargava and B. M. Reddy, *RSC Adv.*, 2013, **3**, 12963–12974.
42 Y. Guo, G. Z. Lu, Z. G. Zhang, S. H. Zhang, Y. Qi and Y. Liu, *Catal. Today*, 2007, **126**, 296–302.
43 X. Y. Chen, Y. Liu, G. X. Niu, Z. X. Yang, M. Y. Bian and A. He, *Appl. Catal., A*, 2001, **205**, 159–172.
44 H. Shinjoh, *J. Alloys Compd.*, 2006, **408–412**, 1061–1064.
45 Z. P. Qu, Y. B. Bu, Y. Qin, Y. Wang and Q. Fu, *Appl. Catal., B*, 2013, **132**, 353-362.
46 H. Najjar, J. -F. Lamonier, O. Mentré, J. -M. Giraudon, H. Batis, *Appl. Catal., B*, 2011, **106**, 149–159.
47 M. R. Morales, B. P. Barbero and L. E. Cadus, *Appl. Catal., B*, 2006, **67**, 229-236.
48 D. Delimaris and T. Ioannides, *Appl. Catal., B*, 2008, **84**, 303-312.
49 Y. X. Liu, H. X. Dai, Y. C. Du, J. G. Deng, L. Zhang, Z. X. Zhao and C. T. Au, *J. Catal.*, 2012, **287**, 149-160.
50 Y. J. Zhu, Y. Q. Sun, X. Y. Niu, F. L. Yuan and H. G. Fu, *Catal. Lett.*, 2010, **135**, 152-158.
51 D. Meng, W. C. Zhan, Y. Guo, Y. L. Guo, L. Wang and G. Z. Lu, *ACS Catal.*, 2015, **5**, 5973-5983.
52 I. Atribak, A. Bueno- López, A. García- García and B. Azambre, Phys. Chem. Chem. Phys., 2010, **12**, 13770-13779.
53 S. Cimino, L. Lisi, S. D. Rossi, M. Faticanti and P. Porta, *Appl. Catal., B*, 2003, **43**, 397–406.
54 J. Trawczynski, B. Bielak and W. Mista, *Appl. Catal., B*, 2005, **55**, 277-285.
55 N. Tang, Y. Liu, H. Q. Wang and Z. B. Wu, *J. Phys. Chem. C*, 2011, **115**, 8214-8220.
56 Z. Say, M. Dogac, E. I. Vovk, Y. E. Kalay, C. H. Kim, W. Li and E. Ozensoy, *Appl. Catal., B*, 2014, **154-155**, 51-61.
57 S. J. Huang, A. B. Walters and M. A. Vannice, *J. Catal.*, 2000, **192**, 29–47.
58 B. Klingenberg and M. A. Vannice, *Appl. Catal., B*, 1999, **21**, 19-33.

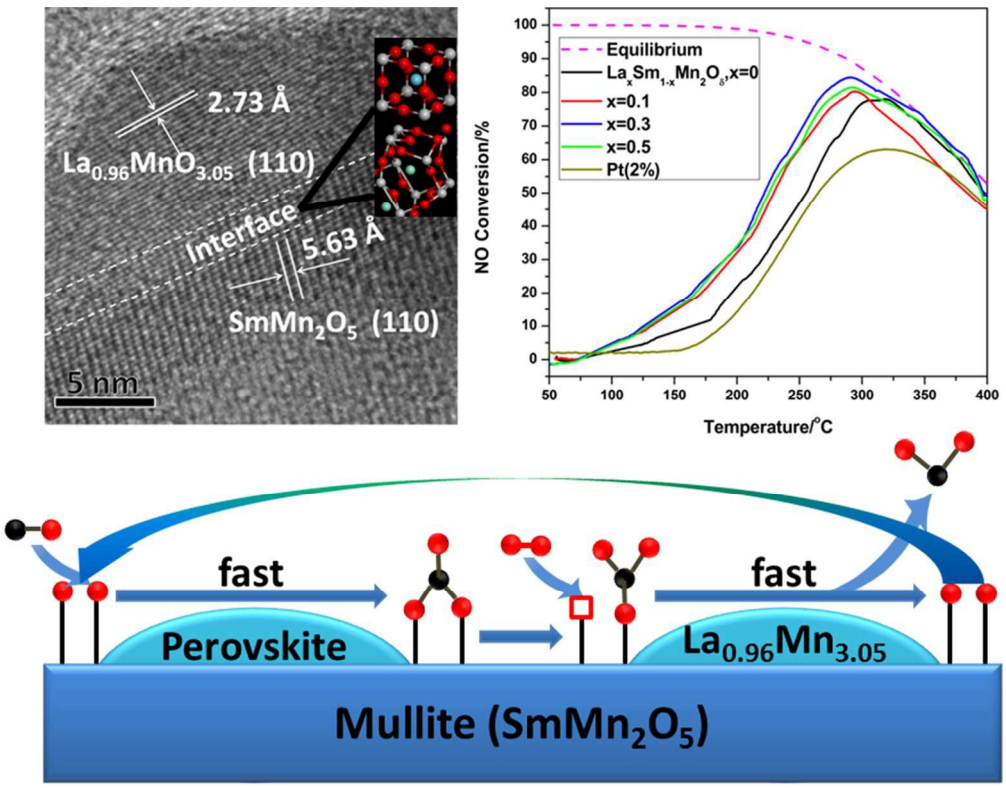

115x89mm (300 x 300 DPI)